Multi-physics joint inversion of field FWI-GPR and ER surface acquired data

Diego Domenzain, Colorado School of Mines; John Bradford, Colorado School of Mines; Jodi Mead, Boise State University*

SUMMARY

We use ground penetrating radar (GPR) and electrical resistivity (ER) surface acquired data on an alluvial aquifer in a multi-physics joint inversion that recovers electrical permittivity and conductivity. Our algorithm is a simultaneous 2.5D joint inversion that coherently integrates the ER data and the full-waveform response of GPR without invoking petrophysical relationships. We join full-waveform inversion (FWI) GPR with adjoint derived ER sensitivities, without the need to interpolate the GPR and ER computational domains. We compare our recovered parameters to individual FWI-GPR and ER recovered parameters. We use capacitive conductivity and neutron-derived porosity borehole measurements to validate our results. Our joint recovered conductivity resembles both control data better than the control data resembles each other, and better than individual FWI-GPR and ER results. Our joint recovered permittivity exhibits subsurface features with higher resolution than that of the FWI-GPR solution.

INTRODUCTION

Accurately quantifying electrical properties of the subsurface is a useful tool for soil characterization (Kaufmann et al., 2020), carbon-dioxide monitoring Carrigan et al. (2013), geothermal exploration Spichak and Zakharova (2015), contaminant detection (Babcock and Bradford, 2015), and groundwater quantity estimation (Parsekian et al., 2012; Beff et al., 2013). As our need to responsibly exploit natural resources grows ever more dire, so does our need to increase the resolution of our estimated subsurface parameters.

We join two different geophysical data: time-domain, full-waveform, multi-offset ground-penetrating radar (GPR), and steady-state electrical resistivity (ER). GPR data are sensitive to electrical permittivity through velocity and reflection, and to conductivity through reflection and intrinsic attenuation. ER data are directly sensitive to electrical conductivity. The spatial-frequency content of the ER data is of longer wavelength when compared to the GPR data. Our method directly exploits this complementary sensitivity of GPR and ER by adding both sensitivities together, and on the same computational grid.

The sensitivities of both data are computed with the adjoint method. This is commonly referred to as full-waveform inversion (FWI) (Tarantola, 1984; Ernst et al., 2007) for GPR. At each iteration, we incorporate the GPR and ER sensitivities using weighted averages. These weights are computed in a data-driven way as a function of the objective function values and several hyper-parameters (Domenzain et al., 2020b). This allows for both the GPR and ER sensitivities to coherently add information during the inversion at all iterations. Moreover, our method accounts for the different depth and spatial-frequency content resolution of both methods during the inversion.

Furthermore, we incorporate the envelope transform of the GPR data into the inversion, and use the cross-gradient constraint to enforce structural similarities (Domenzain et al., 2020a). The cross-gradient constraint is implemented by a decoupled optimization scheme that allows for different confidence weights on either the permittivity or conductivity solution.

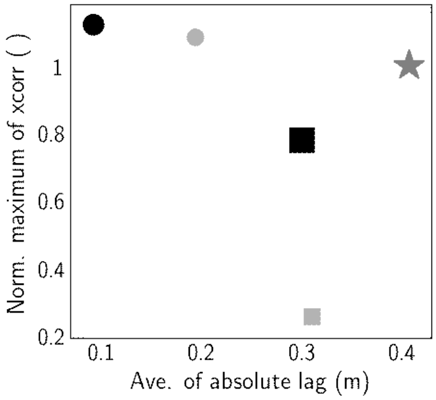

Figure 1: Averages over all boreholes of maximum cross-correlation values (and their respective spatial-lags) of our recovered parameters and borehole measurements of porosity and capacitive conductivity. The maximum cross-correlation values are normalized by the value of porosity cross-correlated with capacitive conductivity, which is denoted by a solid star. Circles and squares denote the ER and GPR inversion results respectively. In black, average values for the joint inversion comparing with the individual inversions. In light gray, average values for the individual inversions.

Here, we present an example of joint inversion (Domenzain et al., 2020a) using FWI-GPR and ER surface acquired field data collected at the Boise Hydrological Research Site (BHRS) (Barrash et al., 1999). We use previous borehole surveys of neutron derived porosity (Barrash and Clemo, 2002), and capacitive conductivity (Mwenifumbo et al., 2009) to compare our recovered parameters. Given that our joint inversion is free from petrophysical assumptions, we do not incorporate any of the borehole measurements in our inversion schemes.

On average over all boreholes, our joint recovered parameters out-perform individual inversions when compared to the control borehole data. Notably, our joint recovered conductivity is a better structural match to both borehole porosity and capacitive conductivity than they are to each other. Both our joint recovered permittivity and conductivity show features with a higher resolution than that of just the GPR and ER recovered parameters. Our method enhances the resolution of subsurface electrical parameters beyond the sensitivities of individual GPR and ER inversions. Figure 1 graphically shows these results.

METHODS

Forward models

Based on previous knowledge of the site (Bradford et al., 2009), we assume the subsurface presents a 2.5D geometry. We consider two-dimensional (Domenzain et al., 2020b) and 2.5-dimensional (Domenzain et al., 2021) forward models for the FWI-GPR and ER experiments respectively. The GPR data are transformed to a two-dimensional record following Bleistein (1986). Both forward models assume 2.5D isotropic physics and 2D model parameters in the xz-plane. Both forward models are discretized on the same computational grid.

Joint inversion

Let $\boldsymbol{\varepsilon}_r$ and $\boldsymbol{\sigma}$ denote the two-dimensional permittivity and conductivity respectively, and $\mathbf{d}^o_w$, $\mathbf{d}^o_{w,a}$ and $\mathbf{d}^o_{dc}$ the GPR data, its envelope, and the ER data respectively. The purpose of our joint inversion is to find positive, two-dimensional $\boldsymbol{\varepsilon}_{r*}$ and $\boldsymbol{\sigma}_*$ such that,

$$\begin{aligned}\{\boldsymbol{\varepsilon}_{r*}, \boldsymbol{\sigma}_*\} = \arg\min \; & \tilde{\Theta}_w(\boldsymbol{\varepsilon}_r, \boldsymbol{\sigma}; \mathbf{d}^o_w, \mathbf{d}^o_{w,a}) \\ & + \Theta_{dc}(\boldsymbol{\sigma}; \mathbf{d}^o_{dc}) + \Theta_\tau(\boldsymbol{\varepsilon}_r, \boldsymbol{\sigma}),\end{aligned} \tag{1}$$

where the residual mean squared (RMS) of the FWI-GPR data and its envelope is denoted by $\tilde{\Theta}_w$, the ER data RMS is given by Θ_{dc}, and the cross-gradient constraint by Θ_τ. Domenzain et al. (2020a) explain in detail each term in equation 1, as well as the optimization procedure with the exception of two modifications: (i) the GPR source estimation routine (Pratt et al., 1998) is introduced within the FWI scheme, and (ii) we compute the 2.5-dimensional ER sensitivities following Domenzain et al. (2021).

All terms being summed in equation 1 influence the updates of $\boldsymbol{\varepsilon}_r$ and $\boldsymbol{\sigma}$ at all iterations. We do not use either $\boldsymbol{\varepsilon}_r$ or $\boldsymbol{\sigma}$ as reference parameters for each other. Rather, we solve for them together in the inversion process. Moreover, both $\boldsymbol{\varepsilon}_r$ and $\boldsymbol{\sigma}$ are discretized on the same computational domain, so no interpolation is needed.

FIELD SITE

The BHRS is located in Boise, Idaho USA, downstream of a nearby irrigation dam that controls the flux of the river throughout the year. The ground surface of the site is dominated by unconsolidated dry gravel that remains dry most of the year but occasionally floods in the springtime. At depth, the site consists of coarse fluvial deposits made up of gravel, sand, and clay that form layered consecutive terraces (Barrash and Clemo, 2002).

Data acquisition

We position our survey line perpendicular to the river. The site is approximately planar with a topographic relief of 0.4m over 36m. The water-table depth measured at the time of the survey was approximately 1m below the ground surface. Both the GPR and ER experiments were performed during the same day and along the same survey line, but not at the same time (about 30 minutes apart).

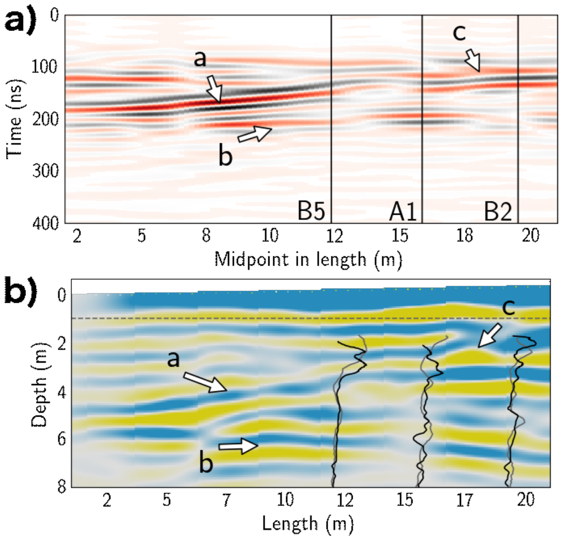

Figure 2: In **a**, common-offset gather of the first receiver in our survey marked with borehole locations. The data were band-passed between 10 and 50 MHz, and gained in time by t^2. Time-zero is when the shot was performed. In **b**, reverse-time migrated reflectivity of the GPR data using our joint recovered parameters. Log data of porosity (gray) and capacitive conductivity (black) are overlaid at borehole positions. The marked events *a, b*, and *c* correspond to the deep edge of the sand channel, and reflectors at ~6m and ~2.5m deep respectively.

We acquired multi-offset GPR data with 50MHz unshielded antennas on a *Sensors & Software, Pulse Ekko Pro* instrument. The ER electrodes were placed along the same line as the GPR experiment. We used an *IRIS Syscal Pro* instrument with a total of 32 electrodes with 1m spacing. All possible dipole-dipole and Wenner arrays were performed.

Figure 2 shows the processed common-offset gather of the first GPR receivers. Events *a, b*, and *c* show strong reflectors that are positioned in depth and recovered by our joint inversion for both permittivity and conductivity.

RESULTS

Recovered conductivity

Figure 3**a-c** shows the recovered conductivity for the FWI-GPR, ER and joint inversions. Given the weak sensitivity of the GPR data to conductivity and our choice of initial model, the recovered conductivity lacks magnitude and low spatial-frequency content. The ER recovered conductivity is able to accurately find the water-table boundary (at ~1m depth), and the water-saturated sand channel expanding inland from the left of the domain. However, the ER solution lacks high spatial-frequency content due to its inherent sensitivity to the subsurface. The joint inversion conductivity shows both low and high spatial-

10.1190/segam2021-3576479.1

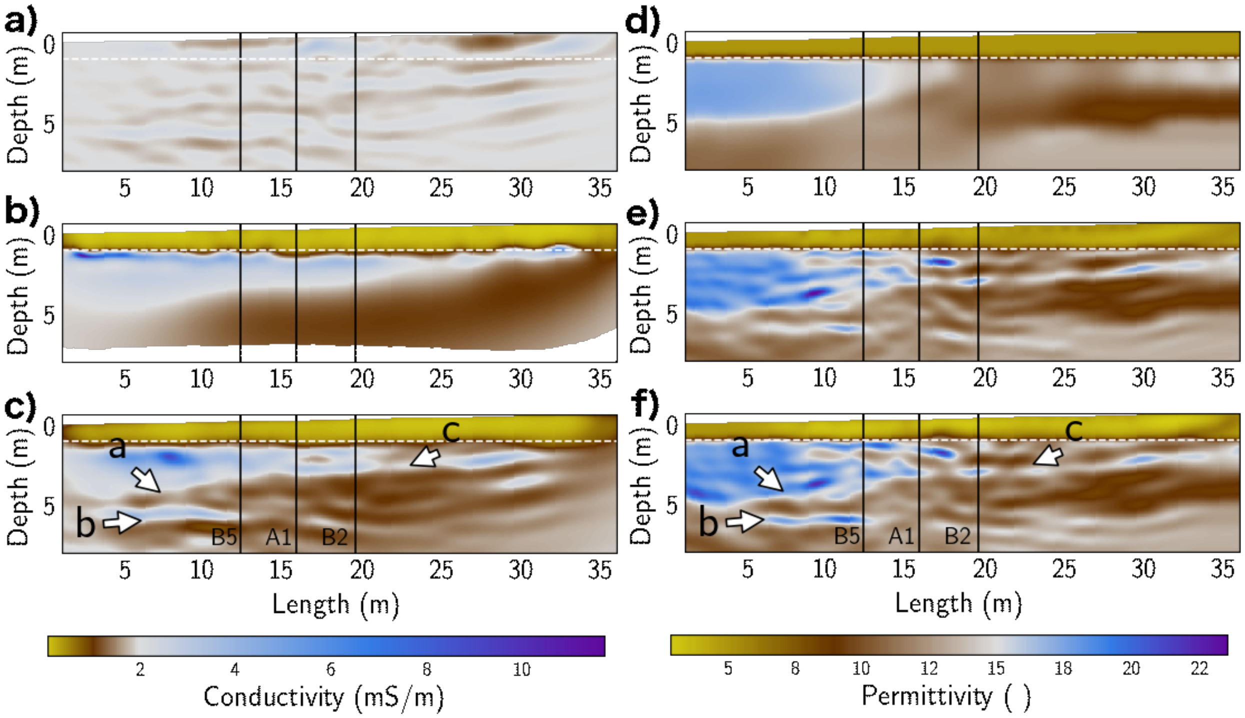

Figure 3: FWI-GPR recovered (**a**), ER recovered (**b**), and joint recovered (**c**) electrical conductivity. The initial conductivity was homogeneous with a value of 2 mS/m. Initial (**d**), FWI-GPR recovered (**e**), and joint recovered (**f**) electrical permittivity.

frequency content. This is due to our joint conductivity update that is able to combine the FWI-GPR and ER sensitivities in a coherent manner into our solution. The marked events *a, b*, and *c* correspond to the deep edge of the sand channel, and reflectors at ~6m and ~2.5m deep respectively.

Recovered permittivity

Figure 3**d-f** shows the initial, FWI-GPR and joint recovered permittivity. Both the FWI-GPR and joint solutions show similar features that are not present in the initial model. Since the cross-gradient constraint was not present in the GPR inversion, the similarities between the FWI-GPR and joint solutions are expressions of only the GPR data. For example, event *c* spanning from borehole B5 at ~3m depth towards 36m in length. The close similarity between the FWI-GPR and joint permittivity solutions is also present in synthetic examples (Domenzain et al., 2020a).

Reflection image

Figure 2**b** shows the reverse-time migrated reflectivity of the GPR data computed with our joint recovered parameters and overlaid with borehole measurements. Figure 2**b** also annotates the reflection events at depth found in the common-offset GPR data in time (Figure 2**a**). The subsurface features that cause these reflection events are also found in our recovered parameters (Figures 3**c** and 3**f**). The annotated event *a* corresponds to the bottom of the sand-channel. The event *b* is the ~6m deep horizon. Lastly, event *c* is the shallow reflector at ~2.5m depth.

Recovered data

Figure 4 shows the GPR observed data (raw and processed),

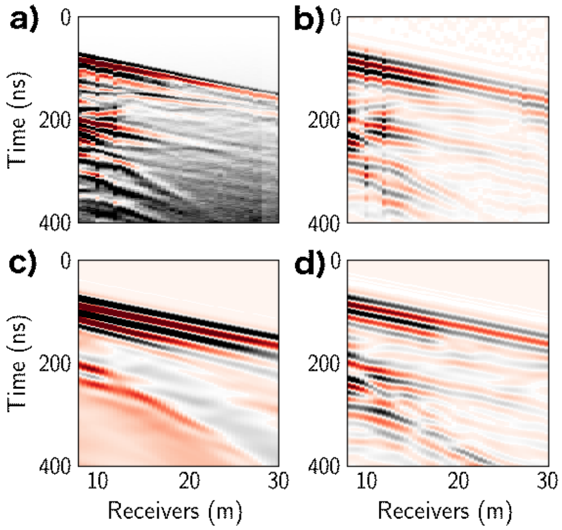

Figure 4: Longest offset GPR shot-gather. Unprocessed (raw) **a**, processed and ready for inversion **b**, initial model **c**, and recovered using joint inversion **d**. Time zero marks the beginning of our forward model. All amplitudes are gained in time by t^2, and clipped to 50% of the maximum and minimum amplitude of the observed and processed data band-passed between 10 and 50 MHz.

computed with initial parameters, and computed with the joint recovered parameters for the longest offset shot-gather in our survey. We note that not all features in the observed data (Figure 4**b**) are present in the initial data (Figure 4**c**). For example, (i) the first arrival event with a linear move-out (at air-speed) is interfered by a shallow reflection event at ~20m; (ii) the event at 200ns is poorly resolved at length; and (iii) the event at ~300ns is not present at all. However, the recovered data (Figure 4**d**) shows all these events.

Figure 5 shows the ER pseudo-sections for the observed, ER recovered, and joint recovered conductivity. They all correspond to the smallest a-spacing dipole-dipole in our survey. Although the ER pseudo-section better resembles the observed data, the joint pseudo-section shows less local variation of apparent resistivity values. For example, among the first 4 n-levels and between n-levels 10 and 20.

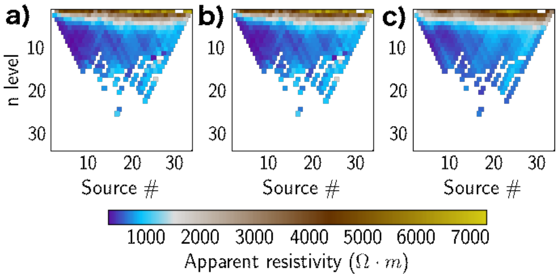

Figure 5: In **a** the processed ER pseudo-section for the dipole-dipole array with a spacing equal to 1m. In **b** and **c** the recovered pseudo-section as in **a** but computed with the recovered ER, and joint conductivity respectively.

Objective functions

Figure 6 shows the history of the objective functions of the individual and joint inversions. Remarkably, the joint FWI-GPR objective function is able to overcome a local minima that the individual FWI-GPR objective function converges to (see Figure 6**a** between 10 and 50 iterations). A similar statement is true for the ER and joint ER objective functions shown in Figure 6**b**: the ER objective function quickly converges to a local minima (in ~10 iterations), whereas the joint ER does not. As a result, the joint solution is able to resolve more subsurface features.

CONCLUSIONS

We present results of a joint, multi-physics, multi-parameter inversion of FWI-GPR and ER field data acquired on the surface. Our joint inversion scheme simultaneously solves for subsurface permittivity and conductivity by using both the GPR and ER sensitivities at each iteration. This means we do not use either the GPR or ER recovered conductivity as reference models in the inversion. Moreover, both FWI-GPR and ER sensitivities are computed on the same discretized domain.

We add the sensitivities of the GPR and ER data in a way that both sensitivities are used at every iteration. This weighting scheme is able to avoid local minima for both the GPR and ER objective functions, resulting in less over-fitting and better subsurface resolution than individual inversions.

Our method does not invoke petrophysical relationships. However, we compare our results to existing borehole measurements of neutron-derived porosity and capacity conductivity data. We find that at borehole locations, the joint recovered parameters are a better match to both the capacitive conductivity and porosity logs, than the porosity and capacitive conductivity logs match each other.

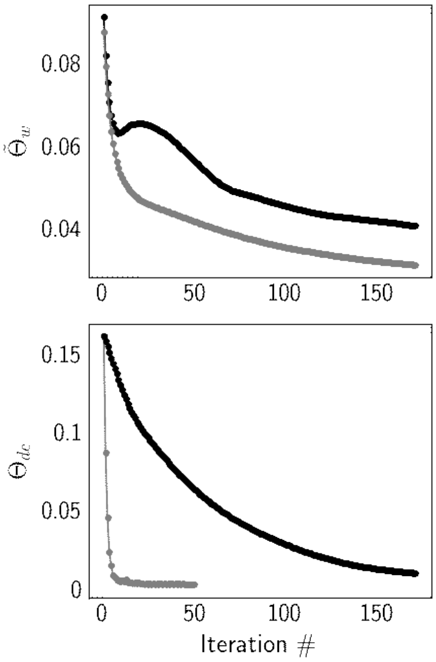

Figure 6: History of the objective function values for our inversions. In black for the joint inversion, and in gray for the individual inversions. In **a** the FWI-GPR (gray) and the FWI-GPR component of the joint (black). In **b** the ER (gray) and the ER component of the joint inversion (black).

10.1190/segam2021-3576479.1

REFERENCES

Babcock, E., and J. H. Bradford, 2015, Reflection waveform inversion of ground-penetrating radar data for characterizing thin and ultrathin layers of nonaqueous phase liquid contaminants in stratified media: Geophysics, **80**, no. 2, H1–H11, doi: https://doi.org/10.1190/geo2014-0037.1.

Barrash, W., and T. Clemo, 2002, Hierarchical geostatistics and multifacies systems: Boise hydrogeophysical research site, Boise, Idaho: Water Resources Research, **38**, 14-1–14-18, doi: https://doi.org/10.1029/2002WR001436.

Barrash, W., T. Clemo, and M. D. Knoll, 1999, Boise hydrogeophysical research site (bhrs): objectives, design, initial geostatistical results: Symposium on the Application of Geophysics to Engineering and Environmental Problems, Society of Exploration Geophysicists, 389–398, doi: https://doi.org/10.4133/1.2922631.

Be, L., T. Guunther, B. Vandoorne, V. Couvreur, and M. Javaux, 2013, Three-dimensional monitoring of soil water content in a maize field using electrical resistivity tomography: Hydrology and Earth System Sciences, **17**, 595–609, doi: https://doi.org/10.5194/hess-17-595-2013.

Bleistein, N., 1986, Two-and-one-half dimensional in-plane wave propagation: Geophysical Prospecting, **34**, 686–703, doi: https://doi.org/10.1111/j.1365-2478.1986.tb00488.x.

Bradford, J. H., W. P. Clement, and W. Barrash, 2009, Estimating porosity with ground-penetrating radar reflection tomography: A controlled 3-D experiment at the boise hydrogeophysical research site: Water Resources Research, **45**, doi: https://doi.org/10.1029/2008WR006960.

Carrigan, C. R., X. Yang, D. J. LaBrecque, D. Larsen, D. Freeman, A. L. Ramirez, W. Daily, R. Aines, R. Newmark, J. Friedmann, et al., 2013, Electrical resistance tomographic monitoring of CO_2 movement in deep geologic reservoirs: International Journal of Greenhouse Gas Control, **18**, 401–408, doi: https://doi.org/10.1016/j.ijggc.2013.04.016.

Domenzain, D., J. Bradford, and J. Mead, 2020a, Joint inversion of full-waveform GPR and ER data. Part 2: Enhancing low frequencies with the envelope transform and crossgradients: Geophysics, **85**, no. 6, H115–H132, doi: https://doi.org/10.1190/geo2019-0755.1.

Domenzain, D., J. Bradford, and J. Mead, 2020b, Joint inversion of full-waveform groundpenetrating radar and electrical resistivity data: Part 1: Geophysics, **85**, no. 6, H97–H113, doi: https://doi.org/10.1190/geo2019-0754.1.

Domenzain, D., J. Bradford, and J. Mead, 2021, Ecient inversion of 2.5 D electrical resistivity data using the discrete adjoint method: Geophysics, **86**, no. 3, E225–E237, doi: https://doi.org/10.1190/geo2020-0373.1.

Ernst, J. R., A. G. Green, H. Maurer, and K. Holliger, 2007, Application of a new 2D time-domain full-waveform inversion scheme to crosshole radar data: Geophysics, **72**, no. 5, J53–J64, doi: https://doi.org/10.1190/1.2761848.

Kaufmann, M. S., A. Klotzsche, H. Vereecken, and J. van der Kruk, 2020, Simultaneous multichannel multi-oset ground-penetrating radar measurements for soil characterization: Vadose Zone Journal, **19**, e20017, doi: https://doi.org/10.1002/vzj2.20017.

Mwenifumbo, C. J., W. Barrash, and M. D. Knoll, 2009, Capacitive conductivity logging and electrical stratigraphy in a high-resistivity aquifer, Boise hydrogeophysical research site: Geophysics, **74**, no. 3, E125–E133, doi: https://doi.org/10.1190/1.3106760.

Parsekian, A. D., L. Slater, and D. Gimenez, 2012, Application of ground-penetrating radar to measure near-saturation soil water content in peat soils: Water Resources Research, **48**, doi: https://doi.org/10.1029/2011WR011303.

Pratt, R. G., C. Shin, and G. Hick, 1998, Gauss–Newton and full Newton methods in frequency–space seismic waveform inversion: Geophysical Journal International, **133**, 341–362, doi: https://doi.org/10.1046/j.1365-246X.1998.00498.x.

Spichak, V. V., and O. K. Zakharova, 2015, Electromagnetic geothermometry: Elsevier.

Tarantola, A., 1984, Inversion of seismic reflection data in the acoustic approximation: Geophysics, **49**, no. 8, 1259–1266, doi: https://doi.org/10.1190/1.1441754.

10.1190/segam2021-3576479.1